AGU PUBLICATIONS

JGR

Journal of Geophysical Research: Oceans

RESEARCH ARTICLE

10.1002/2015JC011343

Optimum interpolation analysis of Aquarius sea surface salinity

Oleg Melnichenko[1], Peter Hacker[2], Nikolai Maximenko[1], Gary Lagerloef[3], and James Potemra[2]

[1]International Pacific Research Center, School of Ocean and Earth Science and Technology, University of Hawaii, Honolulu, Hawaii, USA, [2]Hawaii Institute of Geophysics and Planetology, School of Ocean and Earth Science and Technology, University of Hawaii, Honolulu, Hawaii, USA, [3]Earth and Space Research, Seattle, Washington District of Columbia, USA

Key Points:
- A nearly global, high-resolution SSS product from Aquarius satellite data
- Satellite SSS biases are significantly reduced
- Improved quantification of small-scale features in SSS fields

Correspondence to:
O. Melnichenko,
oleg@hawaii.edu

Citation:
Melnichenko, O., P. Hacker, N. Maximenko, G. Lagerloef, and J. Potemra (2016), Optimum interpolation analysis of Aquarius sea surface salinity, *J. Geophys. Res. Oceans*, *121*, 602–616, doi:10.1002/2015JC011343.

Received 23 SEP 2015
Accepted 15 DEC 2015
Accepted article online 18 DEC 2015
Published online 21 JAN 2016

Abstract A new high-resolution sea surface salinity (SSS) analysis has been produced using Aquarius satellite observations from September 2011 to June 2015. The motivation for the new product is twofold: to produce Level-4 SSS analysis that is consistent with existing in situ observations such as from Argo profile data, and to reduce the large-scale satellite biases that have existed in all versions of the standard Level-3 Aquarius products. The new product is a weekly SSS analysis on a nearly global 0.5° grid. The analysis method is optimum interpolation (OI) that takes into account analyzed errors of the observations, specific to the Aquarius instrument. The method also includes a large-scale correction for satellite biases, filtering of along-track SSS data prior to OI, and the use of realistic correlation scales of SSS anomalies. All these features of the analysis are shown to result in more accurate SSS maps. In particular, the method reduces the effects of relative biases between the Aquarius beams and eliminates most of the large-scale, space-varying, and time-varying satellite biases relative to in situ data, including spurious annual signals. Statistical comparison between the weekly OI SSS maps and concurrent buoy data demonstrates that the global root-mean-square error of the analysis is smaller than 0.2 pss for nearly all weeks over the ∼4 year period of comparison. The utility of the OI SSS analysis is also exemplified by the derived patterns of regional SSS variability.

1. Introduction

The primary objective of this paper is to describe a new high-resolution sea surface salinity (SSS) product derived from satellite observations. The product is a weekly analysis on a near-global 0.5° grid for the period from September 2011 to June 2015. The input data are the Level-2 (L2) swath SSS data provided by the Aquarius/SAC-D satellite, a collaborative space mission between NASA and Argentina's space agency. During its prime mission (25 August 2011 to 7 June 2015), the Aquarius/SAC-D satellite delivered unprecedented space-based observations of SSS with a complete global coverage every 7 days, a significant advance in our ability to monitor SSS variability.

SSS is an important variable that reflects the intensity of the marine hydrological cycle [*U.S. CLIVAR Office*, 2007]. Therefore, knowledge of the spatial and temporal distribution of SSS is essential for understanding the hydrological cycle and for climate monitoring and prediction. Knowledge of the distribution of SSS is also important for better understanding of the ocean circulation and its role in climate [*Schmitt*, 2008; *The CLIVAR Salinity Working Group*, 2008]. Aquarius satellite measurements are capable of achieving high spatial and temporal resolution because of their characteristics, yet they are contaminated by significant instrument noise and also contain large-scale satellite biases and spatially correlated errors [*Lagerloef et al.*, 2015; *Melnichenko et al.*, 2014]. The biases, which are discussed in more detail in later sections, include differences in ascending and descending swath data, interbeam differences, and time-varying biases at annual and shorter time scales [*Lagerloef et al.*, 2015]. In order to improve the utility of Aquarius SSS observations for researchers and application users, the motivation for the new product is twofold: to produce SSS analysis that is quantitatively consistent, at appropriate time and space scales, with existing in situ observations such as those from Argo profile data, and to significantly reduce the large-scale biases that have existed in all versions of the standard Aquarius products.

The possibility of correcting for various errors in Aquarius SSS data by incorporating available statistical information about the signal and noise into the mapping procedure commonly known as optimal interpolation (OI) was tested in a recent study by *Melnichenko et al.* [2014]. The trial analysis in the North Atlantic

demonstrated the utility of the OI technique and the potential of Aquarius SSS products to document salinity structure at fine spatial (∼150 km) and temporal (1 week) resolution with an accuracy of 0.2 pss (salinity is reported on the Practical Salinity Scale 1978 [*UNESCO*, 1985]) or better. The new near-global analysis described in this paper is also based on OI, yet with an additional step to correct the satellite SSS retrievals for large-scale spatial biases using in situ data.

The rest of the paper is organized as follows. Section 2 provides an overview of the satellite SSS data and describes quality control procedures applied to the data. Section 2 also describes the bias correction algorithm. Section 3 briefly describes the interpolation method, focusing on important features of the OI SSS analysis. Section 4 presents examples of the global SSS distribution. Results of the formal validation of the analysis with in situ data are included in section 5. Regional examples of weekly OI SSS fields are then presented in section 6 to illustrate the utility of the product. The paper concludes with a summary of the results and a discussion of limitations and possible improvements of the analysis in section 7.

2. Satellite SSS Data, Data Quality Control, and Correction for Satellite Biases

2.1. Satellite SSS Data

Aquarius/SAC-D is a satellite mission focused on measuring SSS from space. The satellite is positioned on a polar sun-synchronous orbit crossing the equator at 6 P.M. (ascending) and 6 A.M. (descending) local time with a repeat cycle of 1 week. The Aquarius instrument consists of three passive microwave radiometers that "look" along three beams at different angles relative to the sea surface. The beams form three elliptical footprints on the sea surface (76 × 94 km, 84 × 120 km, and 96 × 156 km) aligned across a ∼390 km wide swath. The emission from the sea surface, measured by the radiometers as an equivalent brightness temperature, is converted to SSS, subject to corrections for various geophysical effects [*Wentz et al*., 2012]. A detailed description of the Aquarius/SAC-D satellite mission and the Aquarius instrument can be found in *Le Vine et al*. [2007] and *Lagerloef et al*. [2008].

The satellite observations of SSS used in this study are obtained from Level-2 (L2) version 4.0 Aquarius data produced by the NASA Goddard Space Flight Center's Aquarius Data Processing System (ADPS). The L2 data files, distributed by the Physical Oceanography Distributed Active Archive Center (PO.DAAC) of the Jet Propulsion Laboratory (JPL), contain retrieved SSS, navigation data, ancillary fields, quality flags, and other related information such as sea surface temperature (SST) and surface winds. The data are structured as a sequence of files, each corresponding to one orbit of Aquarius. Each orbit is defined as starting when the satellite passes the South Pole. Individual observations along each orbit consist of a sequence of data points sampled at a 1.44 s (∼10 km) interval. Each individual observation represents the average salinity in the upper 1–2 cm layer and over a ∼100 km footprint [*Le Vine et al*., 2007; *Lagerloef et al*., 2008].

In order to produce the gridded product, the L2 SSS data are first checked for quality. All observations are discarded if they fail any of the following quality flags: 12 (nonnominal navigation), 13 (radiometer telemetry), 14 (roughness correction failure), 16 (pointing anomaly), 17 (brightness temperature consistency), 19 (radio-frequency interference (RFI)), and 21 (reflected radiation from Moon or Galaxy). In the case of flags 19 and 21, the data are excluded from the analysis if the conditions indicated by the flags are either moderate or severe. For other flags, only severe conditions resulted in data rejection. Also excluded from the analysis are data points that are contaminated by land (land fraction > 0.005) or sea ice (sea ice fraction > 0.005); or sampled during high wind (wind speed > 15 m/s) or in cold water (SST < 5°C). A detailed description of the Aquarius quality flags including recommended thresholds can be found in the Aquarius V4.0 Data User Guide (ftp://podaac-ftp.jpl.nasa.gov/allData/aquarius/docs/v4/AQ-010-UG-0008_AquariusUserGuide_DatasetV4.0.pdf).

2.2. Satellite Bias Correction

The next step in data processing consists of a large-scale adjustment of the satellite data relative to in situ data. Analysis of long time series of Aquarius SSS data revealed that satellite retrievals contain large-scale biases relative to in situ data. Their spatial distributions show clear zonality with large negative biases (up to −0.2 pss) in the tropics and positive biases at high latitudes [*Hacker et al*., 2014; *Lagerloef et al*., 2015]. The causes of the biases in Aquarius data are believed to be related to SST-dependent errors in the dielectric

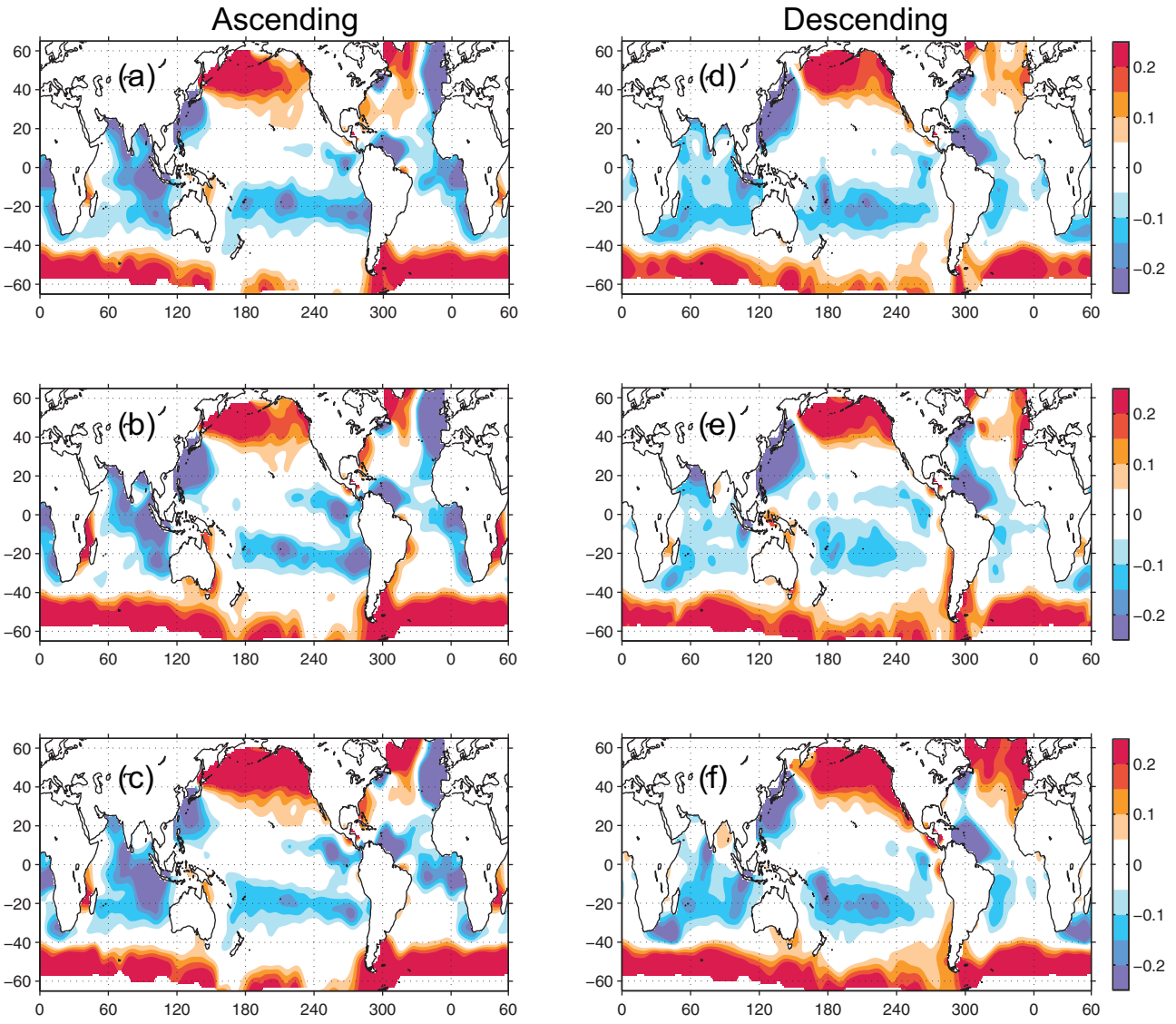

Figure 1. Mean spatial bias correction fields (pss) for Aquarius (left) ascending and (right) descending data; (top) beam 1, (middle) beam 2, and (bottom) beam 3.

constant and the model for atmospheric oxygen absorption, which are part of the retrieval algorithm [*Meissner et al.*, 2015].

In the OI analysis, satellite biases are corrected relative to in situ salinity data collected by Argo floats. The bias fields were constructed by differencing the 5 m Argo salinity and Aquarius-derived SSS fields. The latter were derived using only ascending or only descending satellite observations and also separately for each of the three Aquarius beams. For this purpose, because of the large-scale spatial structure of the bias fields [*Hacker et al.*, 2014], the large-scale SSS fields from Aquarius were constructed by bin averaging of raw Aquarius observations within 6° × 6° spatial bins centered on a global grid with the grid spacing of 3° in both longitude and latitude directions. The Argo-derived fields, which we regard as the "ground truth" at large spatial scales, are monthly mean SSS fields obtained with variational interpolation of Argo buoy measurements. (The gridded Argo product is produced by the Asia-Pacific Data Research Center (APDRC) of the University of Hawaii; available at http://apdrc.soest.hawaii.edu/projects/argo/.) Only systematic, time-averaged biases are taken into account. Thus, there are six bias fields, shown in Figure 1. In order to suppress the unwanted small-scale signals, arising primarily from irregular sampling, the bias fields were smoothed with a two-dimensional running Hanning window of half-width of 8°, generally consistent with

the smoothness properties of the Argo-derived salinity fields. Of note, only the first 3 years of Aquarius observations from September 2011 to August 2014 were used to construct the bias fields (Figure 1).

The spatial variability in the bias fields is significant throughout the ocean (Figure 1). The largest positive biases with magnitudes greater than 0.2 pss are observed in the subpolar North Pacific and in the Southern Ocean. The largest negative biases are observed in the tropics, particularly in the Indian Ocean. Figure 1 also demonstrates that the satellite biases can be different for ascending and descending satellite passes. For example, a large region in the North Atlantic next to Europe is biased low in the ascending satellite data, which is consistent with the effect of RFI contamination from adjacent land areas [*Lagerloef et al*., 2015]. Thus, correcting for the large-scale satellite biases separately for the ascending and descending satellite passes may help reduce the effect of RFI contamination overlooked by the standard RFI detection algorithm. Likewise, correcting for the large-scale satellite biases separately for each of the three Aquarius beams may help reduce residual interbeam biases (this effect has been determined a posteriori), which persist even after applying a multiyear average.

The bias-adjusted satellite observations S_{adj} are determined from the retrieved values S_{obs} as:

$$S_{adj} = S_{obs} - \Delta S, \tag{1}$$

where the bias ΔS is determined by interpolating the bias fields, shown in Figure 1, into the locations of the satellite measurements according to the corresponding Aquarius beam and ascending/descending mode.

The final step in data preparation consists of filtering the data along track to suppress high-frequency instrument noise. The filter is a low-pass Hanning filter of half-width of ~60 km (6 times the along-track sampling). The effect of filtering of the along-track SSS data is illustrated in *Melnichenko et al*. [2014]. From the spectral analysis of along-track SSS data, it has been determined that the instrument noise is essentially white in nature and can effectively be reduced by averaging over a sufficient number of observations. Hanning filter of 60 km half-width, which corresponds to averaging over 12 adjacent observations, has been found to perform quite well to considerably reduce the instrument noise, yet preserve the ocean signal from oversmoothing (see *Melnichenko et al*. [2014, Figure 4], for details). According to the degree of filtering, the SSS data are then subsampled every third point along track.

3. OI SSS Analysis

As in *Melnichenko et al*. [2014], the analysis algorithm is optimal interpolation (OI) applied to quality-controlled and preprocessed Aquarius L2 data. The OI analysis [*Gandin*, 1965; *Bretherton et al*., 1976] uses a background or first guess field, relative to which the observation increments are computed. At each analysis grid point, the analysis increment is estimated as a weighted sum of the observations that influence the grid point, where the weights are optimized to minimize the estimation error variance. This also involves defining error and signal covariances for the input data, which are assumed to have zero mean relative to a given background field. The grid point analysis is completed by adding the analysis increment to the first guess.

The interpolation expression for OI can be written as [*Bretherton et al*., 1976; *Le Traon et al*., 1998]:

$$\hat{S}_x = S_x^0 + \sum_{i=1}^{N}\sum_{j=1}^{N} A_{ij}^{-1} C_{xj}\left(S_i^{obs} - S_i^0\right), \tag{2}$$

where $\hat{S}_x$ is the interpolated value (or estimate) at the grid point $\mathbf{x}$; S_x^0 is the forecast (or "first guess") value at the grid point $\mathbf{x}$; S_i^{obs} ($i=1,\ldots,N$) is the measured value at the observation point i: $S_i^{obs} = S_i + \varepsilon_i$, where ε_i is random measurement error; S_i^0 is the forecast value at the observation point i; $\mathbf{A}$ is the $N\times N$ covariance matrix of the data:

$$A_{ij} = \langle (S_i - S_i^0)(S_j - S_j^0)\rangle + \langle \varepsilon_i \varepsilon_j \rangle, \tag{3}$$

and $\mathbf{C}$ is the joint covariance of the data and the field to be estimated:

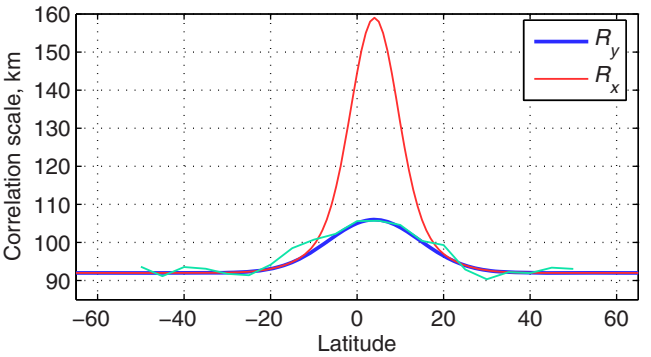

Figure 2. Meridional (blue) and zonal (red) correlation scales applied in the OI SSS analysis. The green curve shows the along-track correlation scales determined by fitting the Gaussian model to the sample covariances estimated in 10° latitude bins from the Aquarius L2 data as described in *Melnichenko et al.* [2014].

$$C_{xj}=\langle(S_x-S_x^0)(S_j-S_j^0)\rangle. \quad (4)$$

In equations (3) and (4), it is assumed that the error and the signal are not correlated.

The error covariance model for the Aquarius along-track data is introduced in the following form:

$\langle\varepsilon_i\varepsilon_j\rangle=\delta_{ij}\sigma_w^2+\sigma_L^2$ if data points i,j are on the same track and beam, and in the same cycle, and

$\langle\varepsilon_i\varepsilon_j\rangle=\delta_{ij}\sigma_w^2$ otherwise,

where δ_{ij} is the Kronecker delta function, σ_w^2 is the variance of uncorrelated errors, and σ_L^2 is the variance of along-track correlated error.

Thus, the algorithm allows two types of errors to contribute to the elements of the error covariance matrix. The first type is white noise (diagonal elements), representing uncorrelated errors. The second type is introduced as a long-wavelength error (by analogy with altimeter applications [*Le Traon et al.*, 1998]) and is justified in our analysis by the fact that the relative biases between the Aquarius beams correlate over long distances along the satellite tracks [*Melnichenko et al.*, 2014; *Hacker et al.*, 2014]. Each Aquarius beam is modeled as having independent error.

The OI method requires knowledge of the first guess and statistical properties of the field to be analyzed. These components are selected as follows.

1. *First Guess*. The first guess fields are derived from monthly mean SSS fields produced by the APDRC with variational interpolation of Argo buoy measurements. The Argo-derived SSS fields are chosen because they are independent from the analysis of the satellite data and provide unbiased large-scale estimates of the first guess. An example and further discussion are presented in section 4.
2. *Signal Statistics*. The normalized spatial covariance of weekly SSS anomalies is described by the Gaussian function:

$$C(r_x,r_y)=\exp\left(-r_x^2/R_x^2-r_y^2/R_y^2\right), \quad (5)$$

where r_x and r_y are spatial lags in the zonal and meridional directions, respectively, and R_x and R_y are the zonal and meridional correlation scales. This form of the correlation structure is chosen because the resulting covariance matrixes are proven to be always positive definite [*Weber and Talkner*, 1993], which is a strict requirement on the choice of a possible analytical form of the correlation function in the OI analysis [*Gandin*, 1965; *Thiebaux and Pedder*, 1987]. The choice may not be truly optimal in statistical sense because the Gaussian function fails to accommodate all the details of the observed correlation array, particularly negative (oscillatory) lobes. Yet it is suitable, since the correlation scales and the major structure (prior to the first zero crossing) of observed SSS correlations in the Aquarius data are well reproduced by the Gaussian model [*Melnichenko et al.*, 2014].

Both the zonal and meridional correlation scales in (5) are allowed to vary with latitude. The meridional scales have been determined by fitting the Gaussian model to the sample correlations estimated in 10° latitude bins from the Aquarius L2 data as described in *Melnichenko et al.* [2014]. Based on the observed distribution of correlation scales, shown in Figure 2 (green curve), the latitudinal dependency of R_y is approximated by the following functional form:

$$R_y(y)=14\exp\left(-(y-4)^2/225\right)+92 \ \text{ km}, \quad (6)$$

where y is latitude in degrees. Thus, the meridional scales are somewhat larger in the tropics (106 km at 4°N) than at high latitudes (92 km).

The zonal correlation scales at middle and high latitudes are set to equal the meridional scales, while in the tropics they are scaled to represent the zonal elongation of correlations as follows:

$$R_x(y)=R_y(y)(0.5\exp(-(y-4)^2/56.25)+1). \quad (7)$$

Near the equator, the aspect ratio R_x/R_y equals 1.5 ($R_x=$ 160 km at 4°N) and gradually decreases toward higher latitudes (Figure 2). Poleward of about 20°, the correlation function (5) becomes isotropic ($R_x=R_y=92$ km). We note, however, that our assumptions of the zonal correlation scales, including the functional form (7), are somewhat arbitrary and based largely on previous observational studies. In the North Atlantic, for example, *Reverdin et al*. [2007] found that in most regions outside of the tropics the zonal and meridional scales are comparable, while near the equator the zonal scales are ~1.5–2 times larger than the meridional scales. Likewise, *Delcroix et al*. [2005] reported on zonal anisotropy in the characteristic scales for SSS in the tropical Pacific and Indian Oceans.

3. *Error Statistics*. The error covariance consists of two parts: the white noise and long-wavelength error. Given prior filtering of Aquarius L2 SSS data, the variance of the white noise is assumed to be 10% of the signal variance, independent of the geographical location. The long-wavelength error correlation is approximated by the exponential function of the form:

$$C_L(l)=\exp(-l/R_L), \quad (8)$$

where l is the along-track separation distance and $R_L=500$ km is the exponential decay scale. The estimate of R_L is obtained by fitting the curve (8) to the interbeam bias statistics evaluated by comparison of the covariances of the interbeam differences for Aquarius and ancillary SSS data as described in *Melnichenko et al*. [2014].

The variance of the long-wavelength error varies with latitude from about 0.04 pss^2 in the tropics to 0.15 pss^2 at high latitudes [*Hacker et al*., 2014]. Following the latitudinal changes in both the error and signal variances (not shown), the ratio of the error variance to the signal variance, η, is approximated as:

$$\eta=2^*(1-\exp(-y^2/400))/1.43)+0.3. \quad (9)$$

Thus, the relative variance of the long-wavelength error is set to vary from 30% in the equatorial region, where the signal variance is large, to more than 150% at high latitudes, where the error variance is large.

The OI SSS analysis is performed on a 0.5° longitude × 0.5° latitude grid every week from September 2011 to June 2015. The weeks are defined to correspond to the standard Level-3 product produced by ADPS to facilitate the comparison (section 5). The OI SSS analysis is run in a local approximation; namely, only data points in a smaller subdomain around the analysis grid point are used. The radius of the subdomain is defined to be four times the space correlation scale, which allows for accommodating both the signal and error correlations. The local approximation also helps to reduce the effect of spatial inhomogeneity in the signal and error statistics [*Weber and Talkner*, 1993].

4. Global SSS Fields

As an example, Figure 3 presents the global SSS distribution in September 2011 derived from the Argo float observations (Figure 3a) and Aquarius OI SSS analysis (Figure 3b). For a fair comparison with the monthly mean Argo field, the weekly OI SSS maps were averaged over the 4 week period 3–30 September 2011. As expected, both SSS fields exhibit the same large-scale patterns, such as higher salinity in the subtropics in all oceans and lower salinity in the tropics and at high latitudes, particularly in the North Pacific. The largest values of SSS are in the subtropical North Atlantic with a secondary maximum in the subtropical South Atlantic.

There are notable differences between the maps as well. The Argo-derived SSS field is very smooth, which is not surprising, given the sparse coverage of in situ measurements. In contrast, the Aquarius OI SSS map shows a very detailed structure. In particular, the North Pacific intertropical convergence zone (ITCZ) appears as a relatively narrow band of low-salinity water extending all the way across the North Pacific. The most notable feature in the North Atlantic is the plume of low-salinity water extending far offshore off the northeastern coast of South America. The feature is associated with the Amazon River outflow and is present seasonally during summer and fall [*Lentz*, 1995]. These important regional features are well resolved by

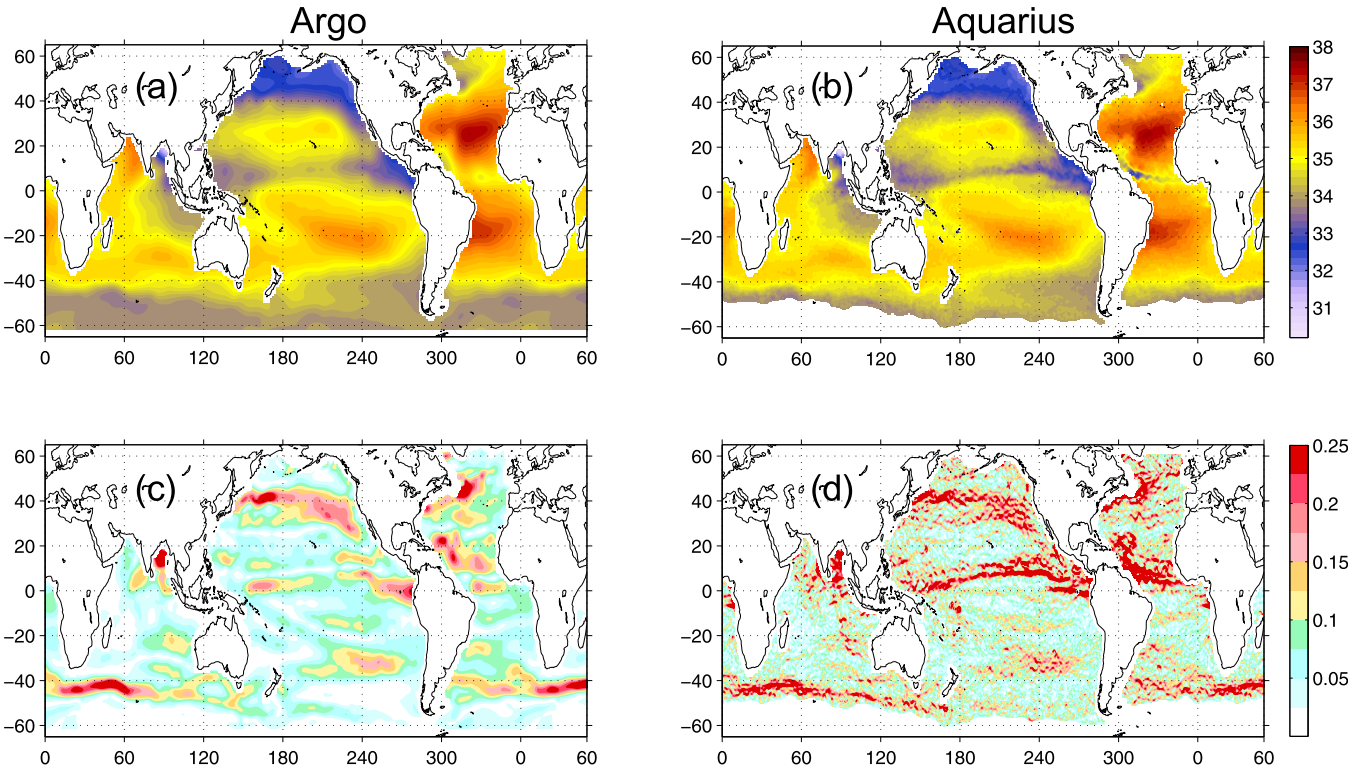

Figure 3. (a) September 2011 mean SSS fields (pss) constructed from in situ Argo float data (first guess for the OI SSS analysis) and (b) OI SSS analysis averaged over the 4 week period 3–30 September 2011. The corresponding gradient fields (pss/100 km) are shown in Figures 3c and 3d.

Aquarius measurements and demonstrate the remarkable achievement of the Aquarius/SAC-D satellite mission [*Lagerloef*, 2012].

The resolution differences between the Argo and Aquarius maps are highlighted by the maps of the magnitude of the horizontal SSS gradient field, shown in Figures 3c and 3d. The SSS gradients are much sharper in the Aquarius OI SSS field compared with the Argo field. Also evident is the fine-scale structure of the fronts revealed by the Aquarius data. For example, undulations of the SSS front are clearly visible along the southern flank of the Amazon River plume in the North Atlantic. The low-salinity band in the tropical North Pacific is flanked by an intense SSS front with local salinity gradients as large as 0.5 pss/100 km. Also, an interesting feature in the eastern part of the subtropical North Pacific is that the broad high gradient region centered at about 35°N, smooth in the Argo-derived map (Figure 3c), appears in the Aquarius OI SSS gradient map (Figure 3d) as a complex system of zonally elongated fronts. This again emphasizes the resolution capabilities of the Aquarius data and OI SSS analysis.

To quantify the magnitude and spatial distribution of SSS variability in the OI SSS analysis, Figure 4a shows the standard deviation of SSS computed from the time series of weekly OI SSS maps over the period from September 2011 to June 2015. Several regions stand out as having the largest SSS variability: the rainy belts (low local salinity, Figure 3b) associated with the ITCZ in the North Pacific and North Atlantic (standard deviations around 0.3–0.5 pss), the South Pacific convergence zone, the eastern equatorial Pacific, the tropical Indian Ocean, the western boundary current regions of the Kuroshio and Gulfstream, the Southern Ocean, as well as the areas near outflows of major rivers, such as the Amazon. Maximum values of the SSS standard deviation, exceeding 1 pss, are observed in the far eastern equatorial Pacific, the Bay of Bengal and Arabian Sea in the Indian Ocean, and the western part of the tropical North Atlantic. Apart from the regions of high SSS variability, the standard deviation of SSS has typical values of around 0.1–0.2 pss.

The standard deviation in Figure 4a includes the large-scale signal and annual cycle. Some part of this variability can be described by the Argo-derived fields, which are used as the first guess for the OI SSS analysis. To quantify the value added by Aquarius, Figure 4b shows the RMS differences (RMSD) between the weekly OI SSS analysis and first guess fields. The largest RMSD, exceeding 0.2 pss, occur in the regions of strong SSS variability

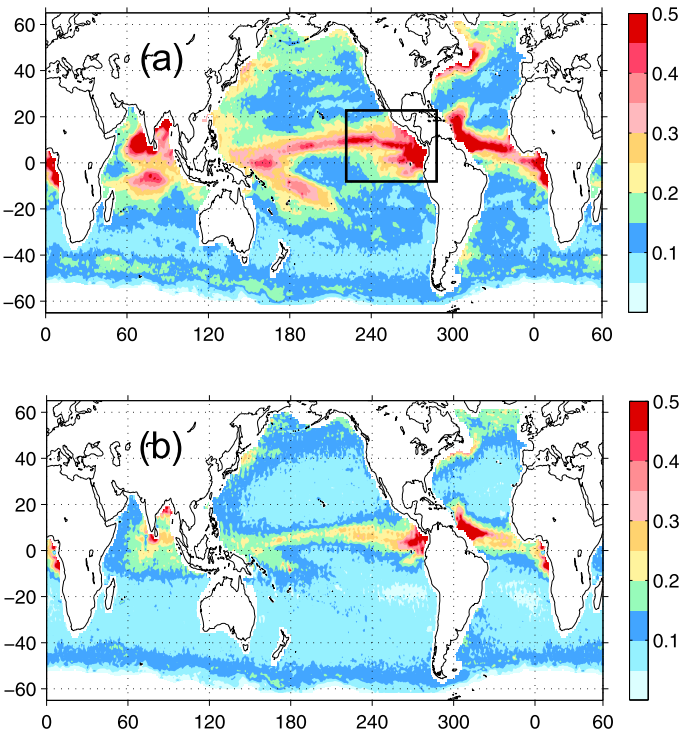

Figure 4. (a) The standard deviation of SSS (pss) computed from weekly time series of OI SSS fields for the period from September 2011 to June 2015. The black box in Figure 4a indicates the area of the regional example described in section 6. (b) The root-mean-square differences between the weekly OI SSS analysis and first guess fields over the period from September 2011 to June 2015.

(Figure 4a), such as around the ITCZ. In some areas, such as the tropical North Atlantic and eastern equatorial Pacific, the SSS RMS variability added by Aquarius exceeds 0.5 pss. These areas are also characterized by strong SSS gradients (Figure 3d). In the subtropical regions, where the SSS gradients are generally weak, the RMS differences between the Argo and Aquarius SSS analyses are less than 0.15 pss.

5. Validation and Intercomparison of SSS Analyses

Following *Melnichenko et al*. [2014], we use Argo buoy observations of salinity in the near-surface layer to estimate the error statistics for various SSS analyses. The Argo buoy network provides quasi-random geographic distribution of about 1100 in situ salinity measurements for each week. Only measurements shallower than 6 m depth and flagged as good from each Argo profile are used in this analysis. The error statistics for the SSS analyses are calculated by comparing buoy measurements for a given week with SSS values at the same locations obtained by interpolating the corresponding Aquarius SSS maps. Two analyses are compared. The first one is the OI SSS analysis described in this paper and the other is the standard Level-3 (L3) SSS product currently produced by ADPS. Of note, the standard 7 day L3 product is constructed by bin averaging of Aquarius L2 SSS data within 1° longitude × 1° latitude spatial bins centered on a regular 1° resolution grid. The bin-averaging procedure effectively eliminates high-frequency (white) instrument noise, but fails to correct for correlated errors in Aquarius data and somewhat limits the product resolution.

Figure 5 shows the bias and RMSD of the OI SSS and the standard L3 product evaluated against concurrent Argo buoy observations. Both products yield the time series of the global bias oscillating around zero (Figure 5a). However, the standard deviation of the weekly biases is much larger for the standard Level-3 product (0.029 pss; blue curve) than for the OI SSS analysis (0.01 pss; red curve). The RMSD of the two analyses differ substantially (Figure 5b). On average, the largest RMSD (0.29 pss) is observed for the standard Level-3 product. The OI SSS analysis improves the RMSD by about 55% (0.18 pss). Also note that the RMSD between the OI SSS analysis and concurrent buoy data is smaller than 0.2 pss for nearly each week during the 196 week period of comparison.

The impact of the bias correction can be seen in the zonally averaged differences between the weekly SSS maps and the corresponding buoy data shown in Figure 6. The zonally averaged biases are calculated weekly by averaging these statistics over 5° latitude bands. As might be anticipated from the results in Figure 1, significant biases still exist in the standard L3 product (Figure 6a). The latitude-time distribution shows large negative biases in the tropical band and positive biases at midlatitude and high latitude. Remarkably, large positive biases at high latitudes are observed throughout a year, including winter and early spring, when the upper ocean layer is well homogenized. Therefore, these biases cannot be explained by possible differences between salinity at 5 m depth, measured by a typical Argo buoy, and that at the sea surface, sampled by Aquarius. Besides the residual static bias, there is a clear seasonal cycle in the bias distribution.

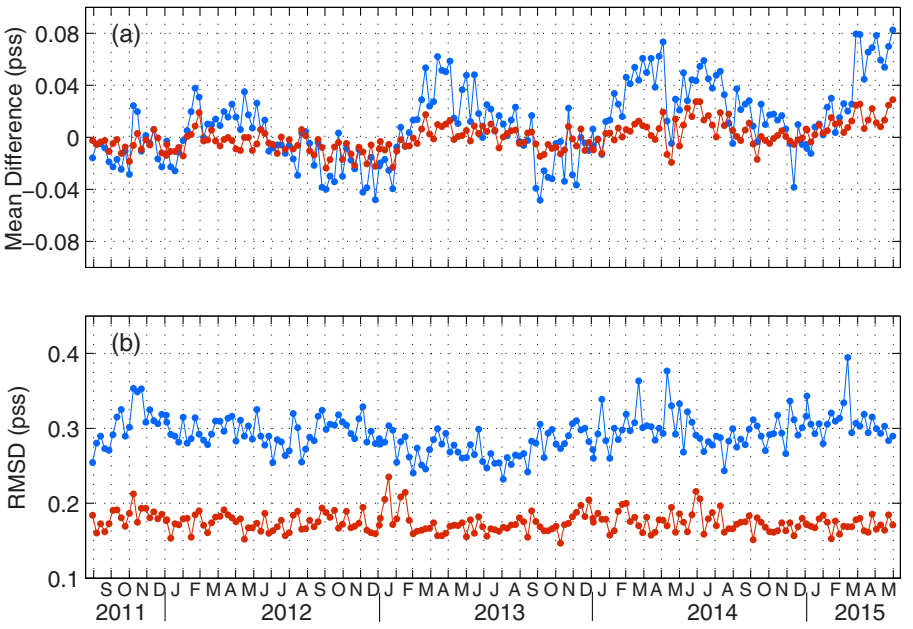

Figure 5. (a) Weekly mean differences and (b) RMSD between Argo buoy observations and two Aquarius SSS analyses: OI SSS (red) and the standard Level-3 SSS product currently produced by the ADPS (blue). The error statistics were computed globally by comparing Argo buoy observations for a given week with SSS values at the same locations obtained by interpolation of the corresponding SSS maps.

Note in particular the asymmetric distribution of the bias relative to the equator with larger negative biases in late winter and early spring in each hemisphere. The causes of the spurious annual signals in Aquarius data are not clear, but are most likely the manifestation of residual geophysical corrections to the measured brightness temperature [*Lagerloef et al*., 2015].

The bias distribution for the OI SSS fields shows nearly zero bias throughout the 196 week period of comparison (Figure 6b). It is worth emphasizing that the original data for the OI analysis have been corrected for only static, time-averaged bias. Yet the seasonal cycle in the bias distribution has considerably been reduced. This effect can be explained by the fact that various types of errors in Aquarius observations are interrelated and, thus, dealing with one type of error (e.g., interbeam biases) inevitably affects other types [*Melnichenko et al*., 2014]. Since the static bias has been removed from the data prior to the OI SSS analysis, the remaining time-varying biases represent correlated errors in the observations with zero mean (as required by the OI analysis) and long spatial correlation scales. In this regard, the long-wavelength error, introduced primarily to correct for relative biases between the Aquarius beams (section 3), also aids in the reduction of the large-scale nonsystematic biases, including spurious annual signals.

Finally, the geographical distribution of the RMSD for the OI SSS analysis is shown in Figure 7. The RMSD were computed in 8° spatial bins from the differences between the weekly SSS maps and collocated Argo buoy observations. The bin size was selected to ensure an adequate number of collocations ($>$100) in each bin. Figure 7 demonstrates that the largest RMSD, exceeding 0.2 pss, are found in the regions of strong variability in SSS (Figure 4a), such as along the North Pacific and North Atlantic ITCZ, the South Pacific convergence zone, the North Pacific subpolar front, the Gulfstream, and near the outflows of major rivers, such as the Amazon in the tropical North Atlantic. However, relatively large discrepancies between the gridded SSS maps and in situ observations in these areas are not necessarily due to errors in Aquarius observations or errors in the mapping procedure. Qualitatively, such a pattern of the mapping error should be expected. In the presence of strong SSS gradients (e.g., Figure 3d), the difference between a point measurement by a buoy and the area averaged SSS sampled by Aquarius can readily exceed 0.2 pss [*Lagerloef et al*., 2010; *Vinogradova and Ponte*, 2013]. The same is true for unresolved temporal variability [*Vinogradova and Ponte*, 2012]. Another source of uncertainty can be related to strong vertical gradients of salinity. In such cases, salinity at 5 m depth, sampled by a typical Argo buoy, may differ significantly from the surface salinity, sampled by Aquarius. Such conditions are frequently observed in the tropics, particularly in the rainy belts associated with the ITCZ [*Schlussel et al*., 1997; *Henocq et al*., 2010].

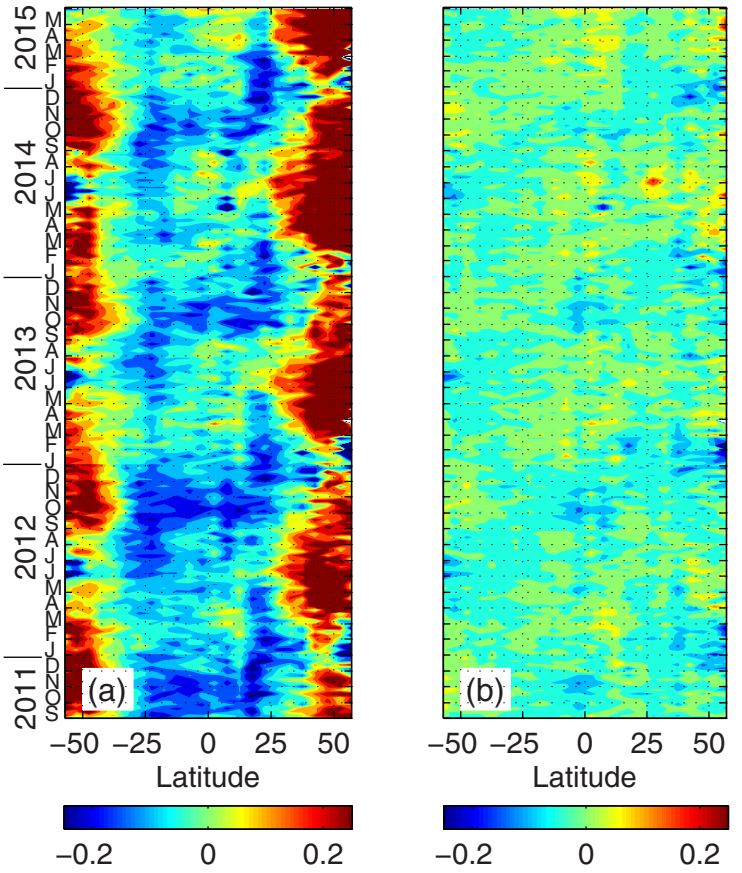

Figure 6. Latitude-time distributions of the zonally averaged differences (pss) between the weekly SSS maps and the corresponding Argo buoy data for two SSS analyses: (a) standard Level-3 product; (b) OI SSS analysis of this paper. The error statistics were computed by comparing Argo buoy observations for a given week with SSS values at the same locations obtained by interpolation of the corresponding SSS maps. The zonally averaged biases were computed by averaging these statistics over 5° latitude bands.

It is worth emphasizing that the OI SSS analysis does not blend in a direct way the satellite and in situ observations such as Argo (see, e.g., *Xie et al*. [2014], for an in situ satellite blended analysis of global SSS). However, the large-scale SSS fields constructed from the Argo buoy observations are used as the first guess fields for the OI analysis of the satellite data. Moreover, these fields are used to construct the bias fields (Figure 1), which, in turn, are used to adjust the satellite retrievals. Given this information, one may conclude that the Argo buoy observations, used for the verification of the OI SSS analysis, are not completely independent of the analysis and may thus result in artificially favorable comparisons between the satellite and in situ salinity at buoy locations.

To demonstrate that this is not the case, we compare each of the two Aquarius SSS products with completely independent thermosalinograph (TSG) salinity data collected by research vessels and Volunteer Observing Ships (VOS). In this study, we use the delayed-mode data provided by the French Sea Surface Salinity Observation Service (http://www.legos.obs-mip.fr/observations/sss/). The data have been subject to vigorous quality control procedures, which included adjustments for any systematic biases in the individual ship tracks (see *Alory et al*. [2015] for a detailed description of the data set). From this data set, only the highest quality SSS values are used to validate the Aquarius products. For consistency with Argo observations, which implicitly contain sampling error due to unresolved temporal and spatial scales, the TSG data are kept at the 5 min (∼2 km) sampling intervals as collected along the ship tracks. Similar to the Argo buoy data, the error statistics for the Aquarius SSS

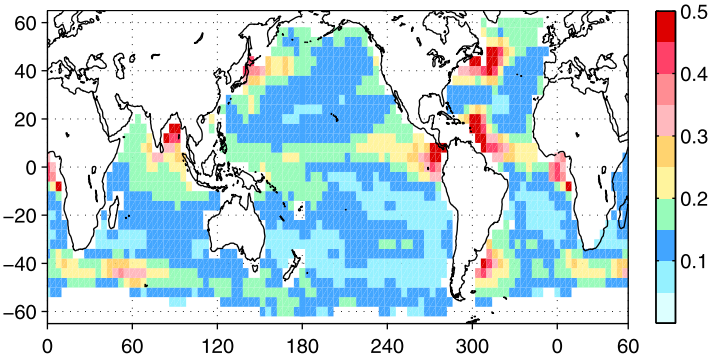

Figure 7. Geographical distribution of the RMS differences (pss) between the weekly OI SSS analysis and in situ buoy data over the period from September 2011 to June 2015. The error statistics are computed in 8° spatial bins by comparing Argo buoy measurements for a given week with SSS values at the same locations obtained by interpolation of the corresponding OI SSS maps.

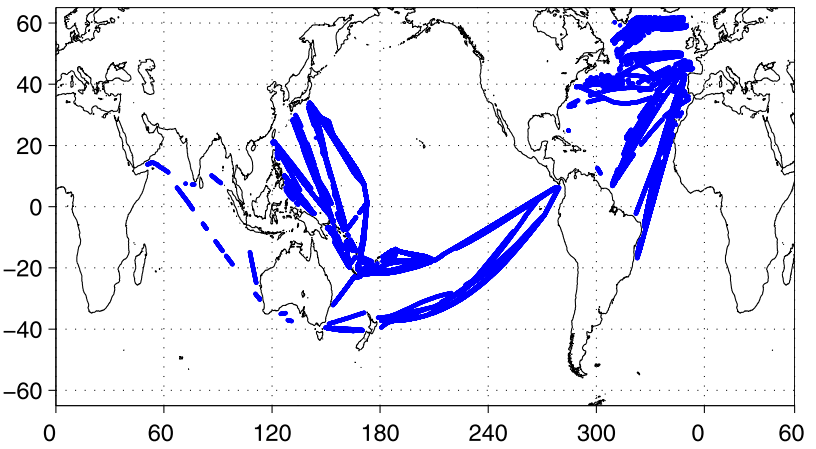

Figure 8. Distribution of VOS-TSG observations from ships for the period from September 2011 to April 2014.

analyses are computed by comparing individual TSG measurements for a given week with SSS values at the same locations obtained by interpolating the corresponding SSS maps.

The distribution of VOS-TSG observations for the period from September 2011 to April 2014 is shown in Figure 8. Unlike the Argo array, the TSG data are very inhomogeneous in both space and time and cover mostly the North Atlantic and western tropical Pacific with just a few lines in the South Pacific and Indian Ocean. As a result, the time series of the bias and RMSD of the two SSS analyses, shown in Figure 9, exhibit significant scatter around the mean values and strongly depend on the weekly distribution of the TSG data. However, the overall tendency for the OI SSS analysis to produce smaller biases and RMSD is evident. On average, the largest RMSD (0.31 pss) is observed for the standard Level-3 product without bias correction, while the smallest RMSD (0.20 pss) is observed for the OI SSS product. These averaged estimates are remarkably consistent with those obtained from the Argo buoy data (Figure 5). A more detailed analysis (not shown here) indicates that the largest differences between the SSS maps and TSG measurements, which

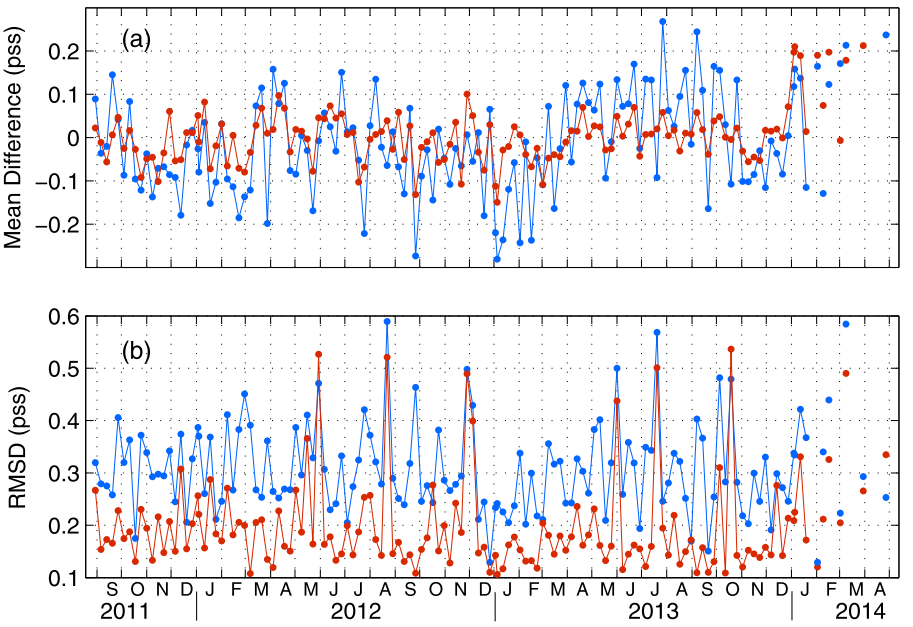

Figure 9. (a) Weekly mean differences and (b) RMSD between VOS-TSG data and two Aquarius SSS analyses: OI SSS (red), and the standard Level-3 SSS product currently produced by the ADPS (blue). The error statistics were computed globally by comparing TSG observations for a given week with SSS values at the same locations obtained by interpolation of the corresponding SSS maps. Each dot in the graph corresponds to 1 week. Only weeks with the number of individual TSG observations greater than 1500 are shown.

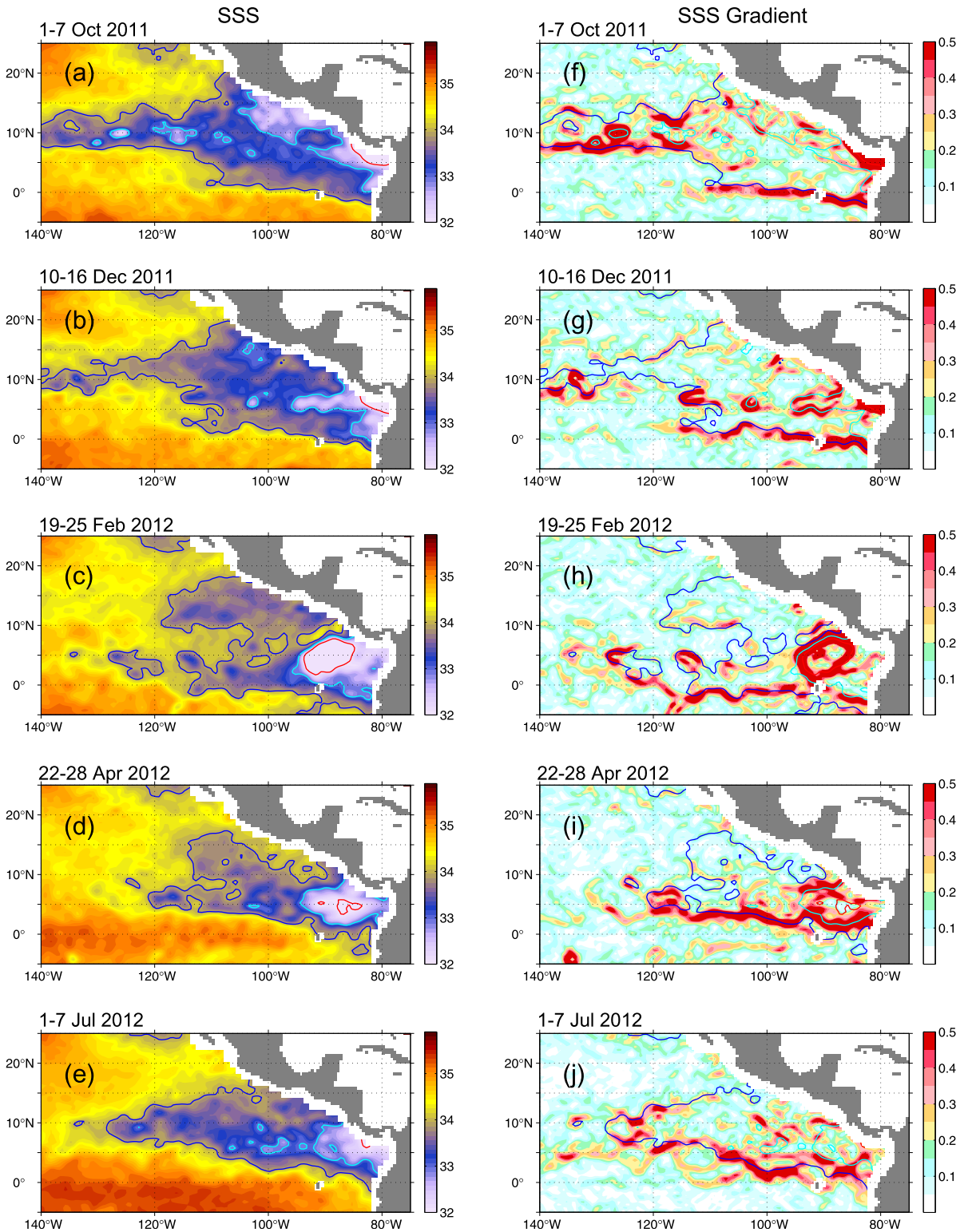

Figure 10. Aquarius OI SSS (pss) in the eastern tropical Pacific for (a) 1–7 October 2011, (b) 10–16 December 2011, (c) 19–25 February 2012, (d) 22–28 April 2012, (e) 1–7 July 2012, and (f–j) the corresponding gradient fields (pss/100 km). Contours are 34 pss (blue), 33 pss (cyan), and 32 pss (red) isohalines.

contribute to the spikes in the RMSD time series (Figure 9b), are observed for the ship tracks located in the area of the Gulfstream extension, near the Amazon River outflow, and in the far eastern equatorial Pacific, generally consistent with Figure 7.

6. Regional Example

The utility of the Aquarius OI SSS data set is further illustrated in this section from example maps of SSS in the eastern tropical Pacific (Figure 10). This region is chosen to demonstrate the capability of the OI SSS product in comparison to recently published analyses of Aquarius SSS [*Yu*, 2014; *Kao and Lagerloef*, 2015] and to generally characterize the SSS variability in the region of the upcoming SPURS-2 field campaign [*SPURS-2 Planning Group*, 2015]. A sequence of weekly SSS maps, covering the period from October 2011 to July 2012, is presented in Figure 10. The times for the plots are chosen somewhat arbitrarily to demonstrate some interesting features in the SSS fields. However, because the large-scale variations in SSS in the region are dominated by the seasonal cycle [*Delcroix et al*., 2005; *Bingham et al*., 2010], the maps also represent typical conditions during a year.

Figure 10a shows the SSS field for the first week in October 2011, a time of year when the ITCZ is at its northernmost annual position [*Xie and Arkin*, 1997; *Yu*, 2015]. A narrow band of low SSS (SSS $<$ 34 pss) is evident along approximately 10°N and is a signature of the zonal band of heavy precipitation in the ITCZ [*Yu*, 2014; *Tchilibou et al*., 2015]. In December 2011 (Figure 10b), the zonal band of low SSS appears to have shifted northward by a few degrees of latitude, apparently due to advection by ocean currents [*Yu*, 2015], but can be a result of a more complicated balance between all the terms in the salinity budget equation, including vertical processes at the base of the mixed layer [*Hasson et al*., 2013]. In this respect, the seasonal migration of the low SSS band in winter is very different from that of the ITCZ rain band (not shown). While the low SSS band progresses further northward and erodes over time, the ITCZ migrates back toward the equator [*Yu*, 2014]. In February 2012 (Figure 10c), substantial new freshening is evident in the zonal band between the equator and 5°N, concomitant with the southernmost annual position of the ITCZ [*Xie and Arkin*, 1997; *Yu*, 2014].

Large seasonal variations in SSS can also be seen along the coast of Central America. This includes the far Eastern Pacific Fresh Pool (EPFP) with SSS lower than 32 pss. The pool is confined to the Gulf of Panama in summer and fall (Figure 10a) and extends far offshore in winter (Figure 10c) in response to regional air-sea-land interactions [*Alory et al*., 2012]. The Aquarius maps also reveal some important smaller-scale features, such as a local SSS maximum around 90°W, 10°N (Figure 10a) associated with the Costa Rica thermocline dome [*Xie et al*., 2005; *Alory et al*., 2012].

The resolution capabilities of the OI SSS maps are best seen from the maps of the SSS gradient field in the right panels in Figure 10, which reveal the fine-scale structure of SSS fronts in the region. The frontal patterns vary over time, generally following the seasonal cycle in SSS [*Kao and Lagerloef*, 2015]. The low SSS belt along 10°N in October 2011 (Figure 10a) is flanked from the south by a sharp SSS front with SSS gradients as large as 0.5 pss/100 km (Figure 10f). The front is present seasonally during summer and fall, when the ITCZ is at its northernmost position, and weakens or disappears in other months [*Kao and Lagerloef*, 2015]. The core of the fresh pool in the far eastern equatorial Pacific (Figure 10c) is flanked by a well-marked SSS front around the 32 pss isohaline (Figure 10h), generally consistent with the analysis of high-resolution TSG data reported by *Alory et al*. [2012]. A quasi-permanent front along the equator, which originates from the coast of South America and extends westward to about 120°W, clearly delineates the boundary between the fresh pool (SSS $<$ 34 pss) to the north and saltier water (SSS $>$ 34 pss) to the south. The location of the front apparently moves only about 3° latitude annually and is well defined by the 34 pss isohaline. Such details of the SSS structure and variability are not available from conventional in situ measurements, thus emphasizing the value added by Aquarius.

7. Summary and Conclusions

The OI SSS analysis of Aquarius L2 (swath) data is produced on a uniform 0.5° longitude/latitude grid at a temporal resolution of 1 week. The analysis method is optimum interpolation that takes into account error information specific to the Aquarius instrument. This includes statistical information on the so-called long-wavelength error that accounts for relative biases between the Aquarius beams, which, if not accounted for, result in artificial north-south striped patterns in mapped SSS fields [*Melnichenko et al*., 2014]. Systematic biases, still present in the Aquarius L2 data, have been considerably reduced in the OI SSS analysis. This is achieved by implementing a new bias correction algorithm that adjusts the SSS retrievals for large-scale systematic (time-averaged) biases. The adjustment is done separately for ascending and descending satellite passes as well as for each of the three Aquarius beams. Such a distinction between the ascending and descending passes helps reduce the effects of

low-level RFI contamination. Further, the use of information on along-track correlated errors contributes to the reduction of nonsystematic biases, including spurious annual signals.

Statistical comparison of the OI SSS analysis with respect to the Argo buoy data showed that the absolute value of the bias, averaged over the global ocean, was smaller than 0.03 pss, while the RMSD was smaller than 0.2 pss for nearly all weeks over the ~4 year period of comparison. The results also show that improvements in the OI SSS analysis are significant relative to the standard L3 product currently produced by ADPS. In particular, the estimated global error of the OI SSS analysis is about 50% smaller than that of the standard L3 product. These estimates are confirmed by further comparisons with completely independent high-resolution TSG data.

Perhaps the most significant result from our analyses is the demonstration that the Aquarius SSS data have provided substantial improvement in our ability to observe nearly globally the small-scale spatial structure (scales $< \sim$1000 km) and its temporal variability (scales $>$ weekly) compared to existing in situ data products. This result will enable the detailed study of small-scale SSS features and their space/time evolution associated with the large-scale variability and processes.

The Aquarius OI SSS analysis is an effort to obtain the best SSS fields from Aquarius observations. A number of improvements are planned in the near future. One of the aspects that need to be addressed is lack of coverage in the coastal regions and semienclosed seas. Data gaps along the coast in the OI SSS analysis are mostly due to exclusion of Aquarius observations that are contaminated by land with the land fraction greater than 0.005. This threshold can probably be relaxed; yet, a thorough study is needed to assess the impact of land on the SSS retrievals and refine algorithms for possible corrections. Another issue in coastal zones and semienclosed seas (i.e., Gulf of Mexico and continental shelf regions), which are lacking Argo observations, is to identify appropriate SSS fields based on in situ data, which can be used as the first guess fields for the OI SSS analysis and/or potential product evaluation. Some other aspects of the OI SSS analysis will also be investigated to improve the quality of the product, including improved estimates of the error and signal covariances. In particular, seasonal and geographical variations in the error and signal statistics are likely worth considering and will be the next step in the analysis.

Digital data of the Aquarius OI SSS analysis are available from the APDRC web page at http://apdrc.soest.hawaii.edu/datadoc/oisss.php (weekly SSS from September 2011 to June 2015).

Acknowledgments

This research was supported by the National Aeronautic and Space Administration (NASA) Ocean Salinity Science Team through grants NNX14AJ02G, NNX12AK52G, and NNX14AJ64G. Additional support was provided by the Japan Agency for Marine-Earth Science and Technology (JAMSTEC), by NASA through grant NNX07AG53G, and by National Oceanic and Atmospheric Administration through grant NA17RJ1230 through their sponsorship of research activities at the International Pacific Research Center (IPRC). Aquarius SSS data are available at ftp://podaac-ftp.jpl.nasa.gov/allData/aquarius/. Argo data were collected and made freely available by the International Argo Program and the national programs that contribute to it (http://www.argo.ucsd.edu). Sea surface salinity data derived from thermosalinograph instruments installed onboard voluntary observing ships were collected, validated, archived, and made freely available by the French Sea Surface Salinity Observation Service (http://www.legos.obs-mip.fr/observations/sss/). The authors acknowledge the many constructive dialogues with members of the Aquarius calibration/validation team. Comments and suggestions by two anonymous reviewers helped improve the quality of the manuscript. This paper is IPRC/SOEST contribution 1164/9561.

References

Alory, G., C. Maes, T. Delcroix, N. Reul, and S. Illig (2012), Seasonal dynamics of sea surface salinity off Panama: The far Eastern Pacific Fresh Pool, *J. Geophys. Res.*, *117*, C04028, doi:10.1029/2011JC007802.

Alory, G., et al. (2015), The French contribution to the voluntary observing ships network of sea surface salinity, *Deep Sea Res., Part I*, *105*, 1–18.

Bingham, F. M., G. R. Foltz, and M. J. McPhaden (2010), Seasonal cycles of surface layer salinity in the Pacific Ocean, *Ocean Sci.*, *6*, 775–787.

Bretherton, F. P., R. E. Davis, and C. B. Fandry (1976), A technique for objective analysis and design of oceanographic experiments applied to MODE-73, *Deep Sea Res. Oceanogr. Abstr.*, *23*, 559–582.

Delcroix, T., M. J. McPhaden, A. Dessier, and Y. Gouriou (2005), Time and space scales for sea surface salinity in the tropical ocean, *Deep Sea Res., Part I*, *52*, 787–813.

Gandin, L. S. (1965), *Objective Analysis of Meteorological Fields*, 242 pp., Isr. Program for Sci. Transl., Jerusalem.

Hacker, P., O. Melnichenko, N. Maximenko, and J. Potemra (2014), Aquarius sea surface salinity observations for global and regional studies: Error analysis and applications, Paper presented at the 2014 Ocean Sciences Meeting, 23–28 February, Honolulu, Hawaii. [Available at http://www.eposters.net/pdfs/aquarius-sea-surface-salinity-observations-for-global-and-regional-studies-error-analysis-and.pdf.]

Hasson, A. E. A., T. Delcroix, and R. Dussin (2013), An assessment of the mixed layer salinity budget in the tropical Pacific Ocean. Observations and modelling (1990–2009), *Ocean Dyn.*, *63*, 179–194.

Henocq, C., J. Boutin, F. Petitcolin, G. Reverdin, S. Arnault, and P. Lattes (2010), Vertical variability of near-surface salinity in the tropics: Consequences for L-band radiometer calibration and validation, *J. Atmos. Oceanic Technol.*, *27*, 192–209.

Kao, H.-Y., and G. Lagerloef (2015), Salinity fronts in the tropical Pacific Ocean, *J. Geophys. Res. Oceans*, *120*, 1096–1106, doi:10.1002/2014JC010114.

Lagerloef, G. (2012), Satellite mission monitors ocean surface salinity, *Eos Trans. AGU*, *93*, 233–234.

Lagerloef, G., et al. (2008), The Aquarius/SAC-D mission: Designed to meet the salinity remote-sensing challenge, *Oceanography*, *20*, 68–81.

Lagerloef, G., et al. (2010), Resolving the global surface salinity field and variability by blending satellite and in situ observations, in *Proceedings of OceanObs'09: Sustained Ocean Observations and Information for Society*, (*Vol. 2*), Venice, Italy, 21–25 September 2009, edited by J. Hall, D. E. Harrison and D. Stammer, ESA Publication WPP-306, doi:10.5270/OceanObs09.cwp.51.

Lagerloef, G., H.-Y. Kao, T. Meissner, and J. Vazquez (2015), Aquarius salinity Validation Analysis; Data Version 4.0, Aquarius Tech. Rep. AQ-014-PS-0016, PO. DAAC, JPL, NASA. [Available at http://podaac.jpl.nasa.gov/SeaSurfaceSalinity/Aquarius.]

Lentz, S. J. (1995), Seasonal variations in the horizontal structure of the Amazon Plume inferred from historical hydrographic data, *J. Geophys. Res.*, *100*(C2), 2391–2400.

Le Traon, P. Y., F. Nadal, and N. Ducet (1998), An improved mapping method of multisatellite altimeter data, *J. Atmos. Oceanic Technol.*, *15*, 522–534.

Le Vine, D. M., G. S. E. Lagerloef, F. R. Colomb, S. H. Yueh, and F. A. Pellerano (2007), Aquarius: An instrument to monitor sea surface salinity from Space, *IEEE Trans. Geosci. Remote Sens.*, *45*, 2040–2050.

Meissner, T., F. Wents, D. LeVine, and P. De Mattheis (2015), Addendum IV to ATBD, Aquarius Tech. Rep. AQ-014-PS-0017, PO. DAAC, JPL, NASA. [Available at http://podaac.jpl.nasa.gov/SeaSurfaceSalinity/Aquarius.]

Melnichenko, O., P. Hacker, N. Maximenko, G. Lagerloef, and J. Potemra (2014), Spatial optimal interpolation of Aquarius sea surface salinity: Algorithms and implementation in the North Atlantic, *J. Atmos. Oceanic Technol.*, *31*, 1583–1600.

Reverdin, G., E. Kestenare, C. Frankignoul, and T. Delcroix (2007), Surface salinity in the Atlantic Ocean (30°S–50°N), *Prog. Oceanogr.*, *73*, 311–340.

Schlussel, P., A. V. Soloviev, and W. J. Emery (1997), Cool and Freshwater skin of the ocean during rainfall, *Boundary Layer Meteorol.*, *95*, 82,437–82,472.

Schmitt, R. W. (2008), Salinity and the global water cycle, *Oceanography*, *21*(1), 12–19.

SPURS-2 Planning Group (2015), From salty to fresh—Salinity Processes in the Upper-ocean Regional Study-2 (SPURS-2), *Oceanography*, *28*(1), 150–159.

Tchilibou, M., T. Delcroix, G. Alory, S. Arnault, and G. Reverdin (2015), Variations of the tropical Atlantic and Pacific SSS minimum zones and their relations to the ITCZ and SPCZ rain bands (1979–2009), *J. Geophys. Res. Oceans*, *120*, 5090–5100, doi:10.1002/2015JC010836.

The CLIVAR Salinity Working Group (2008), What's next for salinity?, *Oceanography*, *21*(1), 82–85.

Thiebaux, H. J., and M. A. Pedder (1987), *Spatial Objective Analysis: With Applications in Atmospheric Science*, 299 pp., Academic Press Inc., London, U. K.

UNESCO (1985), The International system of units (SI) in oceanography, *UNESCO Tech. Pap. 45, IAPSO Publ. Sci. 32*, Paris.

U.S. CLIVAR Office (2007), Report of the U.S. CLIVAR Salinity Science Working Group, *U.S. CLIVAR Rep. 2007-1*, 46 pp., Washington, D. C.

Vinogradova, N. T., and R. M. Ponte (2012), Assessing temporal aliasing in satellite-based surface salinity measurements, *J. Atmos. Oceanic Technol.*, *29*, 1391–1400.

Vinogradova, N. T., and R. M. Ponte (2013), Small-scale variability in sea surface salinity and implications for satellite-derived measurements, *J. Atmos. Oceanic Technol.*, *30*, 2689–2694.

Weber, R. O., and P. Talkner (1993), Some remarks on spatial correlation function models, *Mon. Weather Rev.*, *121*, 2611–2617.

Wentz, F., et al. (2012), Aquarius salinity retrieval algorithm: Algorithm theoretical basis document, Version 2, Addendum I (2012), Addendum II (2013), Addendum III (2014), *RSS Tech. Rep. 082912*, Remote Sens. Syst., Santa Rosa, Calif. [Available at http://podaac.jpl.nasa.gov/SeaSurfaceSalinity/Aquarius.]

Xie, P., and P. A. Arkin (1997), Global precipitation: A 17-year monthly analysis based on gauge observations, satellite estimates, and numerical model outputs, *Bull. Am. Meteorol. Soc.*, *78*, 2539–2558.

Xie, P., T. Boyer, E. Bayler, Y. Xue, D. Byrne, J. Reagan, R. Locarnini, F. Sun, R. Joyce, and A. Kumar (2014), An in-situ-satellite blended analysis of global sea surface salinity, *J. Geophys. Res. Oceans*, *119*, 6140–6160, doi:10.1002/2014JC010046.

Xie, S.-P., H. Xu, W. S. Kessler, and M. Nonaka (2005), Air-sea interaction over the eastern Pacific warm pool: Gap winds, thermocline dome, and atmospheric convection, *J. Clim.*, *18*, 5–20.

Yu, L. (2014), Coherent evidence from Aquarius and Argo for the existence of a shallow low-salinity convergence zone beneath the Pacific ITCZ, *J. Geophys. Res. Oceans*, *119*, 7625–7644, doi:10.1002/2014JC010030.

Yu, L. (2015), Sea-surface salinity fronts and associated salinity-minimum zones in the tropical ocean, *J. Geophys. Res. Oceans*, *120*, 4205–4225, doi:10.1002/2015JC010790.